

Strain-related structural and vibrational properties of thin epitaxial AlN layers

V. Darakchieva* and J. Birch

Department of Physics and Measurement Technology, Linköping University, S-581 83 Linköping, Sweden

M. Schubert

Fakultät für Physik and Geowissenschaften, Universität Leipzig, 04103 Leipzig, Germany

T. Paskova and S. Tungasmita

Department of Physics and Measurement Technology, Linköping University, S-581 83 Linköping, Sweden

G. Wagner and A. Kasic

Fakultät für Physik and Geowissenschaften, Universität Leipzig, 04103 Leipzig, Germany

B. Monemar

Department of Physics and Measurement Technology, Linköping University, S-581 83 Linköping, Sweden

(Received 18 November 2003; revised manuscript received 22 March 2004; published 13 July 2004)

The effect of film thickness on the strain and structural properties of thin epitaxial AlN films has been investigated by high resolution x-ray diffraction techniques and transmission electron microscopy. As a result a sublayer model of the degree of strain and related defects for all films is proposed. A sublayer with low defect density and a strain gradient is found to be present in all films and it reaches a maximum thickness of 65 nm. The films are compressively strained and the strain relaxation after a thickness of 65 nm is shown to be accompanied by misfit dislocation generation and increase of the mosaic tilt. The vibrational properties of the films have been studied by generalized infrared spectroscopic ellipsometry. The proposed sublayer model has been successfully applied to the analysis of the ellipsometry data through model calculations of the infrared dielectric function which confirm the sublayer model. It is found that the strain gradient results in a gradient of the phonon mode frequencies and broadening parameter. The initial strain relaxation in the films leads to narrowing of the observable infrared modes, while further strain relaxation broadens the modes when substantial defect generation occurs.

DOI: 10.1103/PhysRevB.70.045411

PACS number(s): 61.10.Nz, 78.30.Fs, 81.15.Aa, 68.55.Jk

I. INTRODUCTION

Recently, much attention has been focused on AlN because of its attractive physical properties. Due to its high thermal conductivity, high hardness, and stability at elevated temperatures and in caustic environments, AlN is a good candidate for electronic packaging applications. In addition, AlN is considered a promising material for high power optical and surface acoustic wave device applications. AlN also forms a continuous alloy system with GaN, exhibiting a tunable band gap, which is suitable for optical devices operating from blue to the ultraviolet region.¹ In addition, AlN thin films have appeared to be one of the most suitable buffer layers for good quality GaN growth on foreign substrates.²

Despite the recent progress, there are still problems to synthesize the material in the form of high quality epitaxial films.³ Among the different techniques used to obtain AlN, reactive magnetron sputter epitaxy (MSE) provides ultra-high vacuum conditions and excellent opportunities to control the growth process.⁴ Using this technique AlN layers with good crystalline quality and high purity have been grown on SiC.^{4,5} We previously reported that high temperature MSE-AlN has been successfully used as a buffer layer for hydride vapor phase epitaxy (HVPE) of thick GaN layers on sapphire.^{6,7} In contrast to metal organic vapor phase epitaxial GaN grown on low temperature AlN,⁸ no highly

faulted nucleation zone is found in HVPE-GaN grown on high temperature MSE-AlN^{6,7} and the reason is believed to be a specific microstructure of the AlN buffers. Details about the effect of the buffer layer properties on the HVPE-GaN quality and the epitaxial relationship between the AlN films and the substrate were previously reported.^{4,9}

Relatively high dislocation densities, mosaicity, tilted, and twisted small crystallites are well-known characteristics of III-nitride heteroepitaxial layers.¹⁰ Signatures of these defects can be revealed by x-ray diffraction (XRD) techniques. The application of XRD methods for studying III-nitrides presents some challenges because there is an anisotropic distribution of dislocations in the films, related to the wurtzite structure. A broadening of the XRD curves is affected not only by the dislocation structure, but also by heterogeneous strain, impurities, and instrumental broadening. Reciprocal space mapping (RSM) provides an excellent tool for determining defect distribution and degree of strain relaxation in films and heterostructures.¹¹ We note that the studies of the structural properties of thin AlN layers are mostly performed with a focus on the application of the AlN as buffer layers for a subsequent GaN growth.^{4,9,12-14}

Another aspect is the lack of detailed studies of the strain effect on the infrared (IR) vibrational properties of thin AlN layers. We have recently reported on the experimental determination of the $E_1(\text{TO})$ deformation potentials in AlN.¹⁵

However, more information about the parameters of IR active modes is needed, especially for the purposes of modeling the IR response of complex III-V nitride heterostructures, which very often contain a thin AlN buffer layer strained to a different extent^{16,17} or/and an AlN based alloy.¹⁸

In this work MSE-AlN layers on *a*-plane sapphire substrates are studied by high resolution (HR)XRD, transmission electron microscopy (TEM), and generalized infrared spectroscopic ellipsometry (gIRSE). We focus on the evolution of the strain versus layer thickness, and two main relations are investigated: (i) between structural properties and strain and (ii) between vibrational properties and strain. Further, the strain in the films is correlated with the frequencies and broadening parameters of the IR active phonon modes.

II. SAMPLES

AlN layers were deposited on (11 $\bar{2}$ 0)-oriented sapphire (*a*-plane) by reactive dc magnetron sputter epitaxy under ultra-high vacuum conditions ($<5 \times 10^{-9}$ Torr). A 75-mm diameter aluminum disk (purity of 99.999%) was used as a target for sputtering in an atmosphere of purified nitrogen gas (99.99999%) kept at 10 mTorr. AlN layers with thicknesses in the range of 30–110 nm were obtained at a deposition rate of 0.05 nm/s and a constant magnetron target current of 1 A. The substrate-to-target distance was 135 mm and the substrate temperature was kept at 1000°C, as measured by a thermocouple placed behind the substrate. It is difficult to measure the temperature on the surface of a transparent substrate, but it may be lower than 1000°C, due to IR transparency.

III. EXPERIMENTAL AND THEORETICAL PROCEDURES

In order to determine the film thickness we performed low-angle x-ray reflectivity (scattering angle $2\theta \leq 20^\circ$) measurements using a Bragg-Brentano diffractometer with Cu $K\alpha_1$ -radiation, having an instrumental broadening of $<0.05^\circ$. The measured low-angle reflectivity curves were simulated to obtain the film thickness, using the Philips software Win-GIXA.¹⁹ The crystal structure of the AlN buffer layers was investigated by HRXRD using a Philips triple axis material research diffractometer (MRD) system. The possible scan axes are the azimuthal angle ϕ , the tilt angle χ between the scattering vector and the sample surface, the angle 2θ between the incident and diffracted beams, and the “rocking” angle ω . A parabolic graded multilayer mirror collimator, followed by a channel-cut 2-bounce Ge(220) monochromator on the primary side and an asymmetric 2-bounce Ge(220) analyzer crystal giving a resolution of 36 arcsec (around $2\theta=30\text{--}40^\circ$) were used for reciprocal space mapping. The reciprocal space maps (RSMs) were recorded as consecutive coupled $2\theta\text{--}\omega$ scans each separated by an ω offset. Single ω and $2\theta\text{--}\omega$ scans were also measured by a Philips MRD system equipped with a Ge 4-crystal (220) monochromator and a symmetric 2-bounce Ge(220) analyzer in triple axis configuration. The latter gave a resolution of 12 arcsec using Cu $K\alpha_1$ -radiation.

To account for an eventual miscut of the substrate and to provide reproducible measurements the following procedure was employed in the HRXRD and RSM investigations. As a first step the orientations of the AlN $\{10\bar{1}3\}$ planes at grazing angle of incidence were found in an azimuthal ϕ -scan. In this way the reflection planes were brought into the diffraction condition without any χ inclination and therefore a broadening of the rocking curves due to possible azimuthal twist between subgrains is avoided.²⁰ Then the azimuth of the narrowest and strongest peak was chosen. For this fixed azimuth an optimization procedure of the angle of inclination χ was applied by performing successive AlN 0002 ω -scans, each separated by a small χ offset and then a similar ϕ optimization was performed at the AlN $10\bar{1}3$ peak. Finally all angular (ω) and radial ($2\theta\text{--}\omega$) scans, as well as the RSMs were carried out at the optimized χ_{opt} and ϕ_{opt} angles.

Room-temperature gIRSE measurements were performed in the spectral range of 350–1500 cm^{-1} with a spectral resolution of 2 cm^{-1} , and at 70° angle of incidence. Details about the rotating-compensator Fourier-transform-based spectroscopic ellipsometer (J. A. Woollam Co., Lincoln, USA) used are reported in Ref. 21.

The samples were oriented such that the sapphire [0001] axis and the plane of incidence included an angle of approximately 45° . All measurements were performed in the generalized spectroscopic ellipsometry mode, and the spectra of the normalized complex Jones matrix elements R_{pp} , R_{ps} , and R_{sp} defined further below, were determined.

Ellipsometry determines the ratio of the complex reflection coefficients R_p and R_s for light polarized parallel (*p*) and perpendicular (*s*) to the plane of incidence, respectively,²²

$$\rho = R_p/R_s = \tan \Psi \exp(i\Delta), \quad (1)$$

where Ψ and Δ denote the ellipsometric angles. Since both AlN and sapphire are anisotropic materials and because of the *a*-plane orientation of the substrate (the AlN layers are *c*-plane oriented themselves) it is necessary to apply a generalized ellipsometry approach.^{23–25} In the generalized ellipsometry situation Eq. (1) depends on the polarization state of the incident plane wave and the respective parameters Ψ_{ij} and Δ_{ij} ($i, j=p, s$) are defined by the following ratios of the polarized light reflection coefficients:²⁶

$$\frac{r_{pp}}{r_{ss}} = R_{pp} = \tan \Psi_{pp} \exp(i\Delta_{pp}), \quad (2)$$

$$\frac{r_{ps}}{r_{pp}} = R_{ps} = \tan \Psi_{ps} \exp(i\Delta_{ps}), \quad (3)$$

$$\frac{r_{sp}}{r_{ss}} = R_{sp} = \tan \Psi_{sp} \exp(i\Delta_{sp}). \quad (4)$$

A regression analysis is necessary to obtain the IR optical properties from the IRSE data. Further details about the data analysis are given in Refs. 18 and 27 and references therein. The anisotropic AlN dielectric function is parametrized as follows ($j=\parallel$ and $j=\perp$ to the *c*-axis):

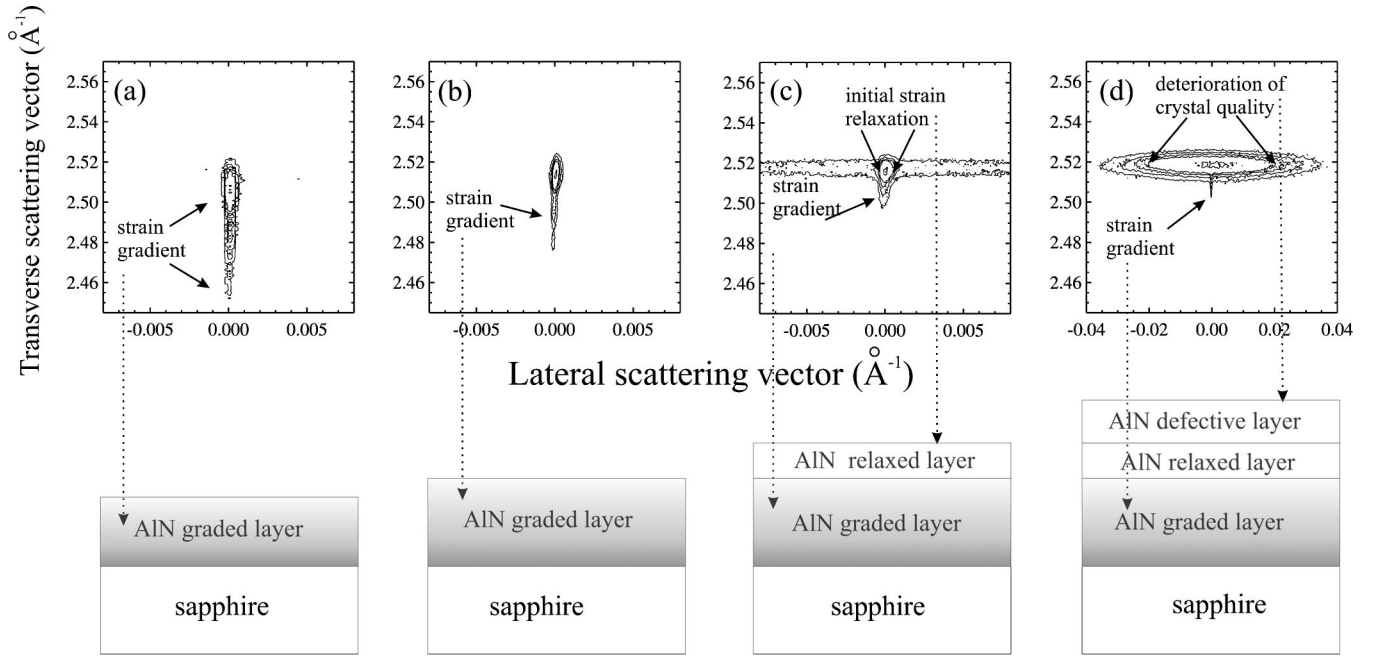


FIG. 1. Reciprocal space maps around the 0002 Bragg peak of AlN layers with different thicknesses: (a) 30 nm, (b) 50 nm, (c) 70 nm, and (d) 110 nm. Note the difference in the lateral scattering vector scales. The intensity is normalized and plotted as 0.9, 0.5, 0.4, 0.3, and 0.2 for all samples measured. Note that the second contour renders the full width at half maximum. Models of the sublayer structure of each film derived from the XRD results are shown for all films below the corresponding map.

$$\varepsilon_j(\omega) = \varepsilon_{\infty,j} \frac{\omega^2 + i\gamma_{LO,j}\omega - \omega_{LO,j}^2}{\omega^2 + i\gamma_{TO,j}\omega - \omega_{TO,j}^2}, \quad (5)$$

where $\omega_{TO,\perp}$, $\omega_{TO,\parallel}$, $\omega_{LO,\perp}$ and $\omega_{LO,\parallel}$ denote the frequencies of the AlN E_1 (TO), A_1 (TO), E_1 (LO), and A_1 (LO) modes, respectively and $\gamma_{TO,\perp}$, $\gamma_{TO,\parallel}$, $\gamma_{LO,\perp}$, $\gamma_{LO,\parallel}$ are the respective broadening parameters. $\varepsilon_{\infty,\perp}$ and $\varepsilon_{\infty,\parallel}$ are the high-frequency limits for polarization perpendicular and parallel to the AlN c -axis.

TEM imaging was performed using a Philips electron microscope operated at 200 kV. Cross-sectional samples were prepared by a conventional procedure including mechanical polishing followed by ion milling to electron transparency. The TEM imaging was performed at imaging conditions (\mathbf{g} , 3g), $\mathbf{g}_{\text{AlN}} = (0002)$.²⁸

IV. RESULTS AND DISCUSSION

A. Strain evolution

The XRD analyses were initiated with $2\theta-\omega$ scans that showed that all films consist of c -oriented crystalline wurtzite AlN with $(0001)_{\text{AlN}} // (11\bar{2}0)_{\text{sapphire}}$. The AlN $10\bar{1}3$ azimuthal ϕ scans of all AlN layers (not shown here) exhibited six-fold symmetry showing that the films are epitaxial with an epitaxial relationship $(0001)_{\text{AlN}} // (11\bar{2}0)_{\text{sapphire}}$ and $[1\bar{1}00]_{\text{AlN}} // [0001]_{\text{sapphire}}$.

Figure 1 shows high resolution reciprocal space maps around the 0002 AlN reciprocal point from films with different thicknesses. A well-resolved main peak and a low-intensity streak in the direction normal to the sample surface

are seen in all RSMs in Fig. 1. The c lattice parameter is determined for each film from the RSM main peak using the transverse scattering vector q_{\perp}

$$q_{\perp} = \frac{4\pi}{\lambda} \sin \theta \cos(\theta - \omega) = \frac{2\pi}{d_{\perp}}, \quad (6)$$

and

$$c = ld_{\perp}, \quad (7)$$

where d_{\perp} is the lattice spacing perpendicular to the film plane and $l=2$ is the respective Miller index. The achieved precision in the determination of the lattice parameter is 2×10^{-5} . The calculated lattice parameters c of all AlN films are larger than the unstrained one for bulk AlN $c_0 = 4.9816 \text{ \AA}$.²⁹ The value of the out-of-plane strain decreases with increasing film thickness from 30 to 110 nm as 0.39, 0.36, 0.25, and 0.15% indicating some partial strain relaxation.

The a lattice parameter was determined for one representative sample from the $10\bar{1}3$ RSM (not shown here) using the lateral scattering vectors q_{\parallel}

$$a = \frac{2\pi}{q_{\parallel}} \sqrt{\frac{4}{3}(h^2 + k^2 + hk)}. \quad (8)$$

We found that the a lattice parameter is smaller than that one of unstrained AlN $a_0 = 3.1130 \text{ \AA}$ (Ref. 29) showing a presence of in-plane compressive strain in the film. Such a biaxial compressive stress is expected to occur in AlN layers on sapphire due to the difference in the thermal expansion coefficients of sapphire and AlN.³⁰ The ratio between the in-plane and out-of-plane strain gives value of 2.1 being

slightly lower than the C_{33}/C_{13} value of 2.8 (Ref. 31). The observed difference can be understood having in mind the uncertainty of the stiffness constants of AlN. Another explanation could in principle be a contribution of hydrostatic strain. However, such contribution should be rather small in our films since previous study on MSE-AlN showed that the films are stoichiometric with low impurity levels.⁴ Hence, we conclude that the in-plane strain in our films is of biaxial compressive nature. The presence of biaxial compressive strain in the films has been confirmed by the observed blue-shift of the $E_1(\text{TO})$ mode frequency with increasing strain.¹⁵

It is seen from Figs. 1(a)–1(c) that the RSMs of 30-, 50-, and 70-nm-thick AlN reveal very narrow main peaks in the direction parallel to the surface plane and elongated in the surface normal direction, which is typical for strained epitaxial layers.³² However, the 0002 peak is twice broader for the 70-nm-thick AlN compared to the 50-nm-thick AlN, indicating that the initial strain relaxation proceeds via misfit dislocation formation or/and increase of the tilt component [Figs. 1(b) and 1(c)]. An additional lattice distortion in this film could be inferred from the broadening of the low-intensity RSM component in lateral direction. The 0002 peak of the 110-nm-thick AlN is considerably broadened in the direction parallel to the surface plane. The observed peak shape is characteristic for a relaxed single crystalline film with a distorted lattice resulting from a generation of misfit relaxation dislocations.³²

The low-intensity streak in all the RSMs in Fig. 1 appears at lower scattering vectors than the main peak. This implies that the scattering comes from a “sublayer” with larger c lattice parameters than that one of the main layer, i.e., the “sublayer” is more strained. The streak is elongated in the direction perpendicular to the sample surface suggesting a strain gradient along the growth direction. A strain gradient in thin AlN layers on sapphire has previously also been observed by XRD using synchrotron radiation.³³ On the other hand no diffuse scattering can be seen around the streak (Fig. 1) indicating that the gradual change of the lattice parameter is not accompanied by a generation of structural defects. Such a strain relaxation mechanism is based on the diminishing of the lattice mismatch as a result of atomic rearrangements and may include a change of stoichiometry.³⁴ The presence of a strain gradient in our films is also manifested in their radial scans. Figure 2 shows single $2\theta-\omega$ scans for the AlN films with different thicknesses. The shift of the main peak toward larger scattering angles indicates a strain relaxation, while the presence of an additional low-intensity peak at the low-angle side of the main peak can be associated with a strain gradient in the films. Figure 3(a) shows the $2\theta-\omega$ scan of the 50-nm-thick film together with a simulation curve obtained using the software *Epitaxy 3.0* provided by Philips. The simulation is performed for strained AlN with thickness of 49.5 nm which agrees well with the x-ray reflectivity results about the film thickness of 50 nm. The x-ray reflectivity measurement and the respective simulation curve are given in Fig. 3(b). As seen from Fig. 3(a) there is higher scattered intensity at the low-angle side of the peak only in the experimental scan which is a direct indication of the presence of a strain gradient in the film. In addition, interference fringes can also be seen in the experimental radial scan. They can be

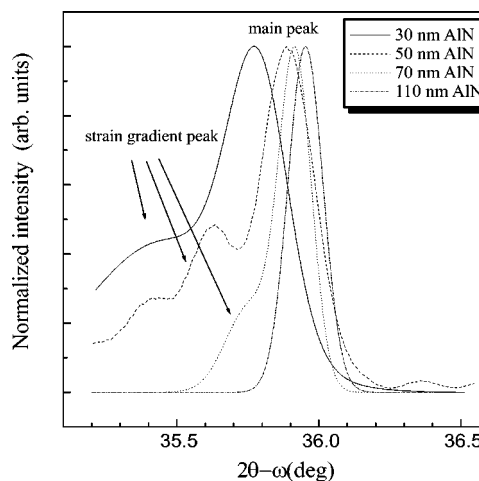


FIG. 2. $2\theta-\omega$ scans of the 0002 Bragg peak of AlN layers with different thicknesses: 30 nm—solid line, 50 nm—dashed line, 70 nm—dotted line, and 110 nm—dash-dotted line. The main peak and the strain gradient peak are indicated.

detected only in relatively thin layers with a high crystal quality and parallel interfaces. This result is in agreement with the RSM results [Fig. 1(b)] showing a peak which is narrow in the direction parallel to the sample surface, and it is also consistent with the abrupt and parallel interfaces, observed by high resolution transmission electron microscopy.⁷ It is seen from Fig. 2 that the intensity of the strain gradient peak decreases appreciably with increasing thickness as compared to the main peak intensity. Moreover, the strain gradient peak can hardly be detected in the single scan of the thickest AlN film. This evolution with film thickness indicates that the highly strained graded “sublayer” appears most probably at the interface with the substrate in order to accommodate the large lattice mismatch. Therefore, based on the RSM and single scan XRD analysis we suggest that the observed low-intensity streak in the RSMs could be attributed to the presence of an interfacial layer with low defect density and a strain gradient along the growth direction.

B. Strain and structural properties

The full width at half maximum (FWHM) variation of the AlN 0002 ω peak with film thickness is shown in Fig. 4. One can see a minimum in the dependence around 50 nm and after that the FWHM increases from 20 to 3240 arcsec with increasing AlN thickness up to 110 nm. The broadening of the 0002 rocking curve indicates an increase of mosaic tilt and density of dislocations with a screw component and a line component along the [0001] direction.³⁵ In principle, the broadening of the 0002 rocking curve could also be due to a presence of domains with small lateral sizes. It is unlikely to have such a contribution to the broadening in our case, since a domain boundary annihilation is usually observed with increasing film thickness.³⁶ Our results suggest that for MSE-AlN on sapphire the critical thickness needed for misfit dislocations to appear and consequently to relieve the strain, is between 50 and 70 nm. It has been shown that the

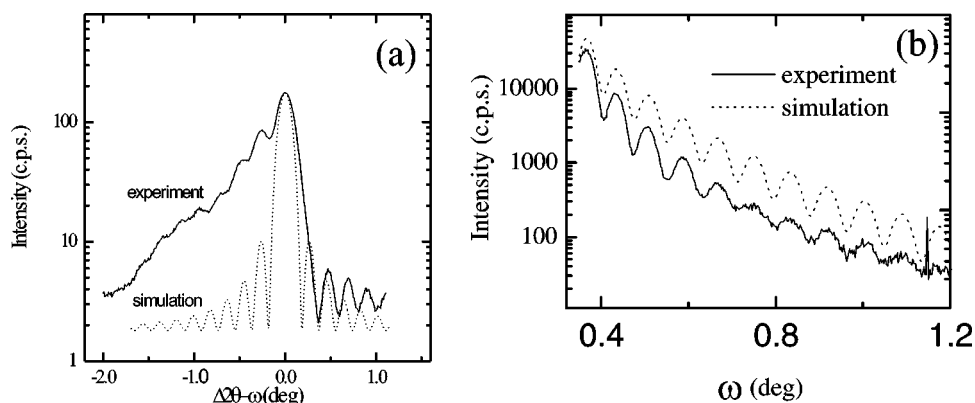


FIG. 3. (a) Experimental (solid line) and simulated (dotted line) $2\theta-\omega$ scan over the 0002 peak of the 50-nm-thick AlN film (note the log scale). Convolution with the x-ray optics broadening is included in the simulation. (b) Experimental (solid line) and simulated (dotted line) x-ray reflectivity curves of the 50-nm-thick AlN film.

critical thickness in the case of metal organic vapor phase epitaxial AlN layers on sapphire is less than 90 nm.³⁷ In contrast to the 0002 rocking curves the asymmetric $10\bar{1}3$ ω peaks of all AlN layers are very broad, with FWHMs typically around 4000 arcsec, measured without the symmetric analyzer (for intensity reasons). In this measuring geometry broadening due to finite thickness is superimposed with the ω -broadening due to structural defects. A broadening due to finite thickness effects would be at most 1200 arcsec as estimated from the transverse widths of the $10\bar{1}3$ peak, which is much less than the observed FWHMs. Therefore, the observed large values of 4000 arcsec could be related to the presence of defects. The peak widths of the asymmetric reflections $hkil$ planes with h and/or k nonzero are affected by the density of threading edge dislocations and the mosaic twist.³⁵ An azimuthal twist (twist axis parallel to the c -axis) broadens all reciprocal lattice points circumferentially around the c -axis. Then, for the the $10\bar{1}3$ peak, which is measured without any inclination of the surface normal with respect to the substrate plane, the twist broadening is perpendicular to the scattering plane and thus do not contribute to the rocking curve width.²⁰ Therefore, the major effect causing the observed $10\bar{1}3$ rocking curve broadening is the density of edge type dislocations. We note that the symmetric rocking curves of the AlN layers are much narrower compared to the respective asymmetric $10\bar{1}3$ peaks. Thus, our results show that the dislocations in the MSE-AlN layers are predominantly of edge type, similarly to earlier observations for GaN grown by HVPE and molecular beam epitaxy.^{20,35}

The broadening of the symmetrical Bragg peaks in radial direction is caused by small coherence lengths in the surface normal direction and heterogeneous strain along the c -axis. These two effects can be separated either by using their different dependency on the diffraction vector or by the different manner they affect the peak shape.³⁸ Using the second method we obtained the structural coherence lengths normal to the surface from the integral 0002 $2\theta-\omega$ peak widths.³⁸⁻⁴⁰ The AlN 0002 $2\theta-\omega$ FWHMs and the corresponding coherence lengths as a function of the film thickness are shown in Fig. 5. The FWHM of the radial scan decreases with increasing AlN thickness indicating an increase of the coherence length. For the 30-nm-thick film the estimated coherence length coincides with the corresponding film thickness (plotted with a solid line in Fig. 5). The coherence lengths of the

50- and 70-nm-thick films are 38 and 56 nm, respectively. These results imply that the $2\theta-\omega$ FWHMs for these samples are mainly limited by the layer thickness and not by crystalline defects. The structural coherence length of the 110-nm-thick AlN is 63 nm suggesting a deterioration of the crystal quality with increasing thickness, as already inferred by the broadening of the rocking curve (Figs. 1 and 4). To further support these XRD findings a TEM study was performed. A TEM weak beam dark-field image of a cross-section of the thickest AlN sample is shown in Fig. 6. Regions with Moire fringes,⁴¹ indicated by arrows, are well resolved in the image. They are caused by the presence of grains with a deviation of their c -axis from the one of the main film and indicates mosaicity in the film. It is seen that the mosaicity increases towards the top surface of the film in accordance with the XRD results showing a distorted crystal quality after a certain thickness (Figs. 1, 4, and 5). In addition, the interfacial region of the layer is apparently free of dislocations and with low density of mosaic regions in agreement with the RSM results. Therefore, we conclude that a layer with a distorted crystal quality is formed on the top of the film after a certain thickness. Based on the RSM, single XRD and TEM results a model of the sublayer structure, characterized by different degrees of strain and defect density can be derived for each film. This is schematically presented in Fig. 1, where the sublayer structure is shown for all

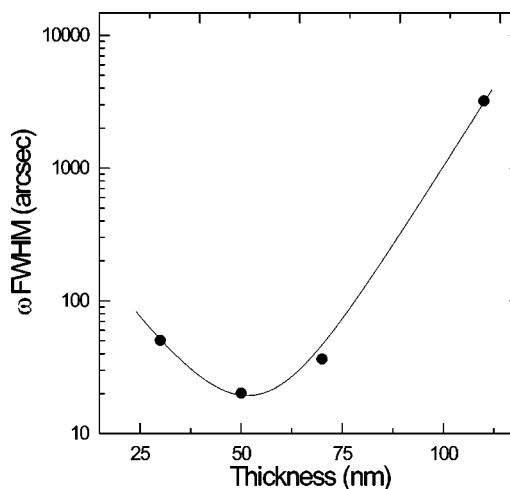


FIG. 4. Full widths at half maximum of AlN 0002 ω scans versus thickness. The line represents only a guide to the eye.

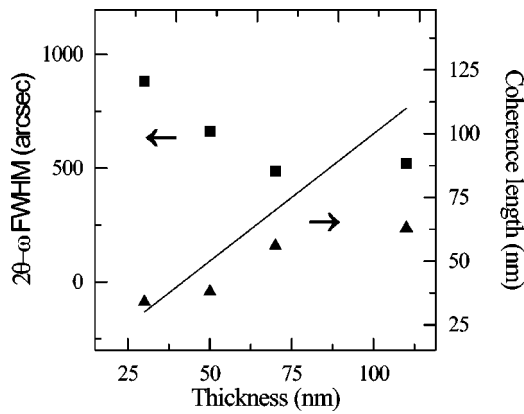


FIG. 5. Full widths at half maximum of AlN 0002 2θ - ω scans (squares) and the corresponding coherence lengths (triangles) as a function of the film thickness. The film thickness is given by the straight line for convenience.

films below the corresponding RSM. All models include an interfacial layer with low defect density and a strain gradient, hereafter called *graded AlN layer* [Figs. 1(a)–1(d)]. A *relaxed layer* is added on the top of the graded layer for the 70-nm-thick film following the XRD findings that an initial strain relaxation via misfit dislocation generation and increase of the mosaic tilt occurs in the film [Fig. 1(c)]. The HR RSM and XRD analysis and the TEM show a deterioration of the structural parameters of the 110-nm-thick AlN layer [Figs. 1(c), 3, and 4], which is accounted for in the model by adding a *defective layer* as shown in Fig. 1(d).

C. Strain and vibrational properties

Figures 7 and 8 show experimental and calculated Ψ and Δ spectra, respectively, for the 30-, 50-, 70-, and 110-nm-thick AlN layers. The off-diagonal elements Ψ_{ps} , Δ_{ps} , and Ψ_{sp} , Δ_{sp} are shown only for the thinnest AlN layer and are not included for the rest of the films for the sake of simplicity. The application of generalized ellipsometry is required since besides the anisotropic dielectric functions and the film thickness, the sample orientation needs to be found.⁴² The off-diagonal elements are mostly needed to locate the exact in-plane orientation of the sapphire *c*-axis during the gIRSE measurements, i.e., the angle that the sapphire *c*-axis includes with the plane of incidence. Prerequisite for the data

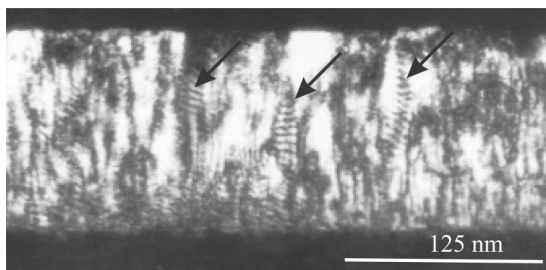


FIG. 6. TEM weak beam dark-field image of the 110-nm-thick AlN film on *a*-plane sapphire. Some of the mosaic domains are indicated by arrows.

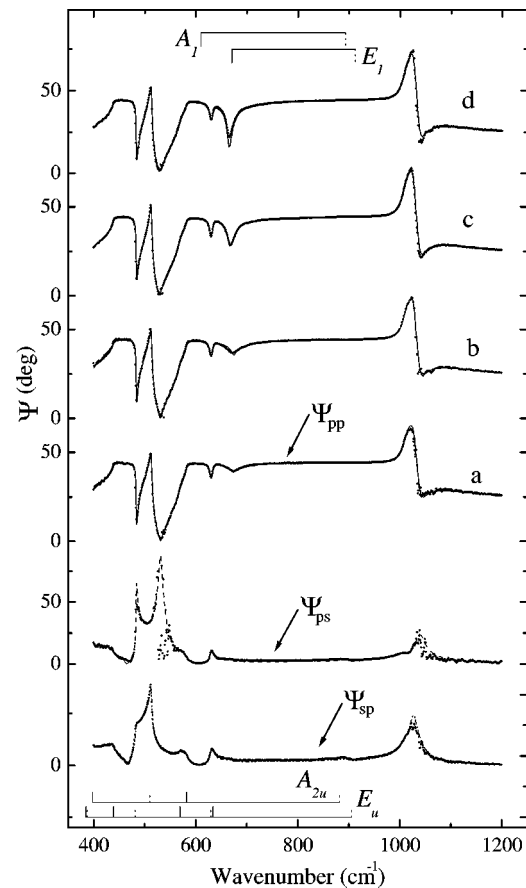


FIG. 7. Experimental (dots) and calculated (solid lines) gIRSE Ψ_{pp} spectra of AlN films with different thicknesses: (a) 30 nm, (b) 50 nm, (c) 70 nm, and (d) 110 nm. The generated Ψ_{ps} and Ψ_{sp} spectra are shown with dashed and dotted-dashed lines, respectively, only for the 30-nm-thick AlN film. The frequencies of the strain-free AlN phonon modes of A_1 and E_1 symmetry, as well as the A_{2u} and E_u phonon modes of sapphire are indicated by vertical lines (solid lines: TO phonons; dotted lines: LO phonons).

analysis is the precise knowledge of the sapphire dielectric functions, which was reported by Schubert *et al.*²⁷ and it was taken without any changes in the present work. To obtain the calculated data for each sample the models derived from the XRD analyses were used. The models were constructed of several “layers” on the base of the respective AlN 0002 RSM, also shown in Fig. 1 above the corresponding model. The model parameters that were allowed to vary during the gIRSE data analysis are the E_1 (TO), E_1 (LO), and A_1 (LO) frequency and broadening parameters, ϵ_∞ , the thickness of each “layer,” and the in-plane orientation of the sapphire [0001]. Due to the *c*-plane orientation of the AlN layers the ellipsometry data are not sensitive to the TO resonance frequency with polarization vector parallel to the sample normal.¹⁸ Consequently, the A_1 (TO) phonon mode resonance could not be found and a value of 611 cm^{-1} (Ref. 31) was used in the calculated data as an input parameter. We used a multiple-sample best-fit procedure which employs a simultaneous minimization of all weighted error functions for each experimental set and the respective model calculation, where all model calculations share a common set of parameters for

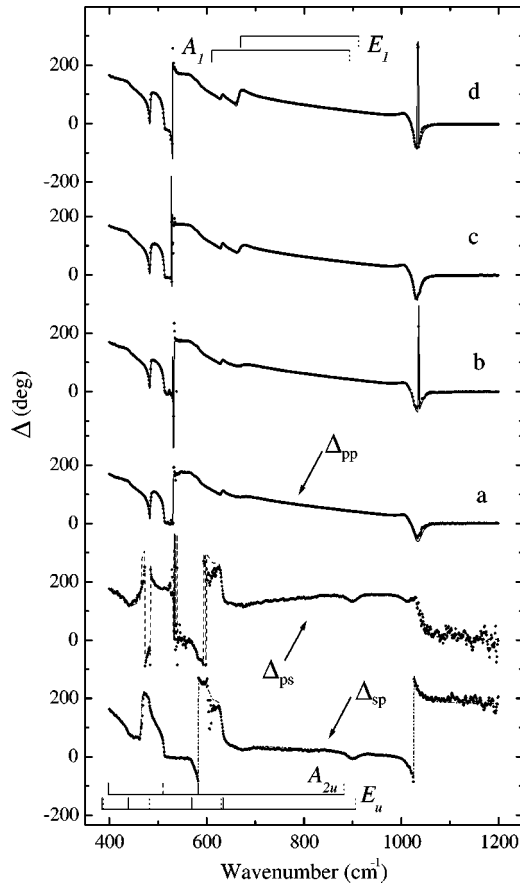


FIG. 8. The same as in Fig. 7 for Δ_{pp} , Δ_{ps} , and Δ_{sp} .

the individual model layer constituents.⁴³ In this way each of the sublayers (graded, relaxed, and defective sublayers) contain common parameters in the models for all samples. The $E_1(\text{TO})$, $E_1(\text{LO})$, and $A_1(\text{LO})$ frequencies and broadening parameters are varied along the thickness of the graded layer in a linear manner. The grading of the IR mode parameters was realized by approximating the graded layer with 12 homogeneous layers. No grading of these parameters is applied for the relaxed and defective layers. In such a way the calculated data for the 30- and 50-nm-thick AlN layers were obtained using a three-phase model: ambient/graded layer/substrate. For the 70-nm-thick film we used a four-phase

model: ambient/relaxed layer/graded layer/substrate. Finally, for the 110-nm-thick AlN film a five-phase model was employed: ambient/defective layer/relaxed layer/graded layer/substrate. We note that the three-phase model could not be applied to the 70- and 110-nm-thick AlN films. In addition, the introduction of a defective layer in the model of the thickest sample significantly improves the agreement between measured and calculated data. These results further justify the proposed sublayer model of the degree of strain and related defect structure.

The gIRSE spectra of the samples are dominated by the reststrahlen bands of sapphire, indicated by the brackets below spectra (a) in Figs. 7 and 8. The sharp peaks in both Ψ and Δ spectra within the sapphire reststrahlen range ($300\text{--}980\text{ cm}^{-1}$) are due to bands of total reflection for the p and s polarized light components between the E_u and A_{2u} phonon modes (for further details see Ref. 27). The lattice modes of the AlN films also affect the Ψ_{pp} and Δ_{pp} spectra. In particular, the gIRSE spectra provide high sensitivity to the frequency and broadening parameter of the AlN $E_1(\text{TO})$ mode. It is seen in Figs. 7 and 8 that for all samples a distinctive spectral feature in Ψ_{pp} and Δ_{pp} appear near the $E_1(\text{TO})$ resonance. The appearance of a spectral feature in Ψ_{pp} related to the $A_1(\text{LO})$ mode has been shown to depend on the film thickness, mode broadening, and layer sequence.⁴⁴ No $A_1(\text{LO})$ related feature is detected for our films. On the other hand, no spectral structure could be directly attributed to the $E_1(\text{LO})$ mode, but both $A_1(\text{LO})$ and $E_1(\text{LO})$ phonon mode parameters can be obtained from the line-shape analysis. Due to the very small thickness of the films compared to the wavelength of the IR probe beam, the IR data have little sensitivity to the anisotropy of the AlN IR optical properties. Therefore, we treated the parameters $\omega_{\text{LO},j}$, γ_j , and $\epsilon_{\infty,j}$ isotropically. The best-fit parameter values for the AlN films are given in Table I. The gIRSE results show that close to the interface with the substrate the AlN $E_1(\text{TO})$ frequency is 692 cm^{-1} (Table I). This value is larger than the strain-free value of 669 cm^{-1} (Ref. 45) indicating the presence of compressive biaxial strain in the films. The result is in agreement with the HRXRD findings about the highly strained interfacial layer with a larger c lattice parameter. With increasing thickness along the graded layer the strain relaxation is manifested by decreasing the $E_1(\text{TO})$ frequency, which reaches a value of 674 cm^{-1} at the top of the

TABLE I. Best-fit values for the high-frequency dielectric constant ϵ_{∞} , the $E_1(\text{TO})$ and (isotropically averaged) LO frequencies, as well as for the phonon mode broadening parameter and the thicknesses of the individual sublayers, according to the gIRSE regression analysis using the sublayer models depicted in Fig. 1.

AlN	ϵ_{∞}	$\omega_{E_1(\text{TO})} (\text{cm}^{-1})$	$\omega_{\text{LO}} (\text{cm}^{-1})$	$\gamma (\text{cm}^{-1})$	Thickness (nm)			
					30 ^a	50 ^a	70 ^a	110 ^a
Graded layer (bottom-top)	3.19 ± 0.03^b	$692 \pm 2 - 674 \pm 2$	$892 \pm 1 - 884 \pm 6$	$160 \pm 3 - 4 \pm 1$	40 ± 1	64 ± 1	65 ± 1	58 ± 5
Relaxed layer	3.80 ± 0.1	669 ± 1	913 ± 2	15 ± 1			15 ± 1	33 ± 2
Defective layer	3.80 ± 0.1	673 ± 2	913 ± 2	68 ± 4				24 ± 3

^aThickness of the whole layer as determined by x-ray reflectivity.

^bParameter not graded.

layer. We note that the $E_1(\text{TO})$ frequency covers a much broader interval of values along the graded layer due to the large broadening parameter. The strain gradient along the graded layer, Δe_{zz} , can be estimated from the RSMs according to Eqs. (6) and (7) and using the strain-free value of the c lattice parameter reported in Ref. 29. Then, in the case of predominant biaxial strain, we estimated the frequency shift of the $E_1(\text{TO})$ mode along the graded layer using¹⁵

$$\Delta\omega_{E_1(\text{TO})} = \left(-a_{E_1(\text{TO})} \frac{C_{33}}{C_{13}} + b_{E_1(\text{TO})} \right) \Delta e_{zz}, \quad (9)$$

where $a_{E_1(\text{TO})}$ and $b_{E_1(\text{TO})}$ are the deformation potentials of the AlN $E_1(\text{TO})$ mode and C_{ij} are the stiffness tensor elements. For C_{33}/C_{13} we used the above obtained value of 2.1. We obtained frequency shifts of 61.4 and 60.3 cm^{-1} , when using the experimentally determined deformation potentials for the $E_1(\text{TO})$ mode in Refs. 15 and 46, respectively. These values are larger than the $E_1(\text{TO})$ frequency shift of 18 cm^{-1} directly obtained from the gIRSE results for the graded layer (see Table I). We note that a possible contribution of hydrostatic strain, related to some stoichiometry change along the graded layer, is not accounted for in Eq. (9). The difference between the estimated values of the $E_1(\text{TO})$ frequency shift and the determined one from the gIRSE can be explained by the uncertainty in the stiffness constants and in the deformation potentials.^{15,46} It is worth mentioning that the experimentally determined deformation potentials of the AlN phonon modes reported so far^{15,46} are based on studies of relatively thin AlN films. Therefore, a presence of a strain gradient that has not been accounted for may influence the determined values and could possibly explain the existent discrepancy between experimentally determined and calculated deformation potentials.^{15,46,47} The broadening parameter also evolves with strain, being much larger at the interface with the substrate and gradually decreasing along the thickness of the graded layer (Table I). In principle, the near-interface region in highly mismatched heterostructures is usually very defective, due to the accommodation of the large lattice mismatch between the substrate and the film.⁴⁸ Therefore, a large value of the broadening parameter close to the interface would not be surprising and could be related to the presence of defects. However, we note that the RSM and TEM results showed that the interfacial sublayers of the films are virtually free of dislocations and with low degree of mosaicity, which we relate to an initial coherent growth of highly strained AlN with a strain gradient. Another possible explanation is that the broadening parameter could be widened in an attempt to mimic a larger strain gradient than the one given by the frequency shift or to account for a possible nonlinear grading. Similar to the $E_1(\text{TO})$ mode, the LO frequency also experiences a shift along the graded layer (Table I).

The $E_1(\text{TO})$ mode in the relaxed layer has a frequency of 669 cm^{-1} coinciding with the strain-free value⁴⁵ and a relatively small broadening parameter of 15 cm^{-1} (Table I). The structural investigations showed that further growth up to a thickness of 110 nm is disturbed by dislocation generation and increase of the degree of mosaic tilt (Figs. 1 and 4–6).

This is manifested in the gIRSE response by an increase of the broadening parameter up to 70 cm^{-1} and the value of the $E_1(\text{TO})$ frequency up to 674 cm^{-1} with respect to the corresponding values for the relaxed layer. The latter could be related to microstructure variation or generation of defects which create strain fields. We note that the generation of strain possibly due to grain growth or island coalescence was detected by *in situ* measurements for thick GaN films.⁴⁹

The total thicknesses of the AlN films determined from the gIRSE results are very close to the values estimated by XRD, being slightly larger. The observed difference is most probably related to the employment of different model parameters in the gIRSE and x-ray reflectivity data simulations. These model parameters (for instance, the material density and the dielectric constant) differ from the bulk values available in the literature and in addition are strongly dependent on the defect structure in a complex manner and may correlate with the film thickness.⁵⁰ The results for the individual thicknesses (Table I) show that a strained growth of high quality material is realized up to a thickness of 58–65 nm, in agreement with the XRD findings that the strain relaxation via misfit dislocation generation occurs between 50 and 70 nm. Further relaxed growth of approximately 25 nm without a significant deterioration of the crystal quality can be achieved. Any further increase of the film thickness is related to substantial defect generation. We note that the thickness value of 58–65 nm of the high-quality strained AlN layer also confirms our previous findings for the optimal buffer thickness for subsequent HVPE-GaN growth.^{6,9}

V. CONCLUSIONS

The strain evolution and its effect on the structural and vibrational properties of thin epitaxial AlN layers with different thicknesses have been studied by HRXRD, TEM, and gIRSE. Based on the HRXRD and TEM results a model of the strain evolution with film thickness and related defect structure is suggested and it is successfully applied to the gIRSE data analysis. A layer with low defect density and a strain gradient is found to be present in all films and has been suggested to form at the interface with the substrate. The strain gradient is manifested in a gradient of the frequency and broadening parameters of the observable IR active modes along the thickness of the graded layer, showing higher strain at the interface which decreases towards the top. All films are compressively strained and partial strain relaxation occurs with increasing film thickness, resulting in narrowing of the IR active modes and shift of the $E_1(\text{TO})$ frequency towards the strain-free value. We found that after a thickness of about 58–65 nm the strain relaxation is accompanied by a misfit dislocation generation, an increase of the mosaic tilt and a decrease of the coherence lengths. Therefore, the critical thickness needed for misfit dislocation generation is estimated to be between 58 and 65 nm. The value of the $E_1(\text{TO})$ frequency of the relaxed layer is found to confirm previous result for AlN single-crystals, while the LO frequency is found to be somewhat higher than both the $E_1(\text{LO})$ and $A_1(\text{LO})$ frequencies of AlN single-crystals. A substantial generation of defects is observed at a thickness of

110 nm which results in broadening of the IR active modes and a small blueshift of the $E_1(\text{TO})$ frequency.

It is worth noting that the results for the degree of strain and related defect density, and the individual thicknesses of

the sublayers deduced from the gIRSE analysis are in good agreement with the HRXRD findings. Therefore, the gIRSE has been demonstrated to be an excellent tool for studying strain evolution in thin films with complex strain behavior.

*Electronic address: vanya@ifm.liu.se

- ¹S. Strite and H. Morkoc, *J. Vac. Sci. Technol. B* **10**, 1237 (1992).
- ²I. Akasaki, A. Amano, Y. Koide, K. Hiramatsu, and N. Sawaki, *J. Cryst. Growth* **98**, 209 (1989).
- ³S. N. Mohammad and H. Morkoc, *Prog. Quantum Electron.* **20**, 361 (1996).
- ⁴J. Birch, S. Tungasmita, and V. Darakchieva, in *Nitrides as Seen by the Technology*, edited by T. Paskova and B. Monemar, p. 421 (Research Signpost, Trivandrum, India, 2002).
- ⁵S. Tungasmita, J. Birch, P. O. Å. Persson, K. Järrendahl, and L. Hultman, *Appl. Phys. Lett.* **76**, 170 (2000).
- ⁶T. Paskova, E. Valcheva, J. Birch, S. Tungasmita, P. O. Å. Persson, P. P. Paskov, S. Evtimova, M. Abrashev, and B. Monemar, *J. Cryst. Growth* **230**, 381 (2001).
- ⁷E. Valcheva, T. Paskova, S. Tungasmita, P. O. Å. Persson, J. Birch, E. B. Svedberg, L. Hultman, and B. Monemar, *Appl. Phys. Lett.* **76**, 1860 (2000).
- ⁸K. Hiramatsu, S. Itoh, H. Amano, I. Akasaki, N. Kuwano, T. Shiraishi, and K. Oki, *J. Cryst. Growth* **115**, 628 (1991).
- ⁹V. Darakchieva, J. Birch, P. P. Paskov, S. Tungasmita, T. Paskova, and B. Monemar, *Phys. Status Solidi A* **90**, 59 (2002).
- ¹⁰S. D. Lester, F. A. Ponce, M. G. Graford, and D. A. Steigerwald, *Appl. Phys. Lett.* **66**, 1249 (1995).
- ¹¹D. J. Dunstan, *J. Mater. Sci.: Mater. Electron.* **8**, 337 (1997).
- ¹²Y.-M. Le Vaillant, R. Bisaro, J. Olivier, O. Durand, J.-Y. Duboz, S. Ruffenach-Clur, O. Briot, B. Gil, and R.-L. Aulombard, *J. Cryst. Growth* **189/190**, 282 (1998).
- ¹³H. Lahrèche, P. Vennéguès, O. Tottreaut, M. Läügt, P. Lorenzini, M. Leroux, B. Beaumont, and P. Gibart, *J. Cryst. Growth* **217**, 13 (2000).
- ¹⁴Z. Y. Fan, G. Rong, J. Browing, and N. Newman, *Mater. Sci. Eng., B* **67**, 80 (1999).
- ¹⁵V. Darakchieva, P. P. Paskov, T. Paskova, J. Birch, S. Tungasmita, and B. Monemar, *Appl. Phys. Lett.* **80**, 2302 (2002).
- ¹⁶M. Schubert, J. A. Woollam, A. Kasic, B. Rheinländer, J. Off, B. Kuhn, and F. Scholz, *Phys. Status Solidi B* **216**, 655 (1999).
- ¹⁷A. Kasic, M. Schubert, J. Off, and F. Scholz, *Appl. Phys. Lett.* **78**, 1526 (2001).
- ¹⁸A. Kasic, M. Schubert, S. Einfeldt, D. Hommel, and T. E. Tiwald, *Phys. Rev. B* **62**, 7365 (2000).
- ¹⁹D. K. G. de Boer, *Phys. Rev. B* **44**, 498 (1991).
- ²⁰T. Paskova, E. Valcheva, J. Birch, S. Tungasmita, P. O. Å. Persson, R. Beccard, M. Heuken, and B. Monemar, *J. Appl. Phys.* **88**, 5729 (2000).
- ²¹T. E. Tiwald, D. W. Thompson, and J. A. Woollam, *J. Vac. Sci. Technol. B* **16**, 312 (1998).
- ²²R. M. A. Azzam and N. M. Bashara, *Ellipsometry and Polarized Light* (North-Holland, Amsterdam, 1984).
- ²³M. Schubert, *Phys. Rev. B* **53**, 4265 (1996).
- ²⁴M. Schubert, B. Rheinlander, J. A. Woollam, B. Johs, and C. M. Herzinger, *J. Opt. Soc. Am. A* **13**, 875 (1996).
- ²⁵M. Schubert, *Thin Solid Films* **313–314**, 323 (1998).
- ²⁶D. W. Berreman and F. C. Unterwald, *Phys. Rev.* **174**, 791 (1968).
- ²⁷M. Schubert, T. E. Tiwald, and C. M. Herzinger, *Phys. Rev. B* **61**, 8187 (2000).
- ²⁸D. J. H. Cockayne, *J. Phys. (Paris), Colloq.* **35**, C141 (1974).
- ²⁹H. Angerer, D. Brunner, F. Freudenberg, O. Ambacher, M. Stuzmann, R. Höpler, T. Metzger, E. Born, G. Dollinger, A. Bergmaier, S. Karsch, and H.-J. Körner, *Appl. Phys. Lett.* **71**, 1504 (1997).
- ³⁰*Landolt-Börnstein*, Vol. 17, edited by O. Madelung (Springer, New York, 1982).
- ³¹V. Yu. Davydov, Yu. E. Kitaev, I. N. Goncharuk, A. N. Smirnov, J. Graul, O. Semchinova, D. Uffmann, M. B. Smirnov, A. P. Mirgorodsky, and R. A. Evarestov, *Phys. Rev. B* **58**, 12899 (1998).
- ³²P. F. Fewster, *Crit. Rev. Solid State Mater. Sci.* **22**, 69 (1997).
- ³³H. Ch. Kang, S. H. Seo, and D. Y. Noh, *Jpn. J. Appl. Phys., Part 1* **38**, 187 (1999).
- ³⁴D. Shilo, E. Lakin, and E. Zolotoyabko, *Phys. Rev. B* **63**, 205420 (2001).
- ³⁵B. Heying, X. H. Wu, S. Keller, Y. Li, D. Kapolnek, B. P. Keller, S. P. DenBaars, and J. S. Speck, *Appl. Phys. Lett.* **68**, 643 (1996).
- ³⁶S. Tungasmita, J. Birch, P. O. Å. Persson, K. Järrendahl, and L. Hultman, *Appl. Phys. Lett.* **76**, 170 (2000).
- ³⁷J. Chaudhuri, R. Thokala, J. H. Edgar, and B. S. Sywe, *J. Appl. Phys.* **77**, 6263 (1995).
- ³⁸T. Metzger, R. Höpler, E. Born, O. Ambacher, M. Stuzmann, R. Stömmmer, M. Schuster, H. Göbel, S. Christiansen, M. Albrecht, and H. P. Strunk, *Philos. Mag. A* **77**, 1013 (1998).
- ³⁹P. Scherrer, *Gött. Nachrichten* **2**, 98 (1918).
- ⁴⁰A. R. Stokes and A. J. C. Wilson, *Proc. Phys. Soc.* **56**, 174 (1944).
- ⁴¹Th. Kehagias, Ph. Komninou, G. Noet, P. Ruterana, and Th. Karakostas, *Phys. Rev. B* **64**, 195329 (2001).
- ⁴²M. Schubert, in *Theory and Application of Generalized Ellipsometry*, Handbook of Ellipsometry, edited by G. E. Irene and H. G. Tompkins (W. Andrew Publ., Noyes Publications, Norwich, USA), in press.
- ⁴³M. Schubert, B. Rheinlander, C. Cramer, H. Schmiedel, B. Johs, C. M. Herzinger, and J. A. Woollam, *J. Opt. Soc. Am. A* **13**, 1930 (1996).
- ⁴⁴A. Kasic, Ph.D. thesis, Leipzig, 2002.
- ⁴⁵M. Kuball, J. M. Hayes, A. D. Prins, N. W. A. van Uden, D. J. Dunstan, Y. Shi, and J. H. Edgar, *Appl. Phys. Lett.* **78**, 724 (2001).
- ⁴⁶J. Gleize, M. A. Renucci, J. Frandon, E. Ballet-Amalric, and B. Daudin, *J. Appl. Phys.* **93**, 2065 (2003).

- ⁴⁷J.-M. Wagner and F. Bechstedt, *Phys. Rev. B* **66**, 115202 (2002).
- ⁴⁸T. Paskova, E. Valcheva, and B. Monemar, *Defect Diffus. Forum* **200–202**, 1 (2002).
- ⁴⁹S. Hearne, E. Chason, J. Han, J. A. Floro, J. Figiel, J. Hunter, H. Amano, and I. S. T. Tsong, *Appl. Phys. Lett.* **74**, 356 (1999).
- ⁵⁰C. M. Herzinger, H. Yao, P. G. Snyder, F. G. Celi, Y.-C. Kao, B. Johs, and J. A. Woollam, *J. Appl. Phys.* **77**, 4677 (1995).